On the Localisation of the FPZ under a Pure Mode II Load Identified by a Hybrid Method.

Authors Names and Affiliations

Petr Miarka[a,b*], Alejandro S. Cruces[c], Pablo Lopez-Crespo[c], Wouter De Corte[d]

[a]Institute of Physics of Materials, Czech Academy of Science, Žižkova 22, 616 00 Brno, Czech Republic

[b]Brno University of Technology, Faculty of Civil Engineering, Veveří 331/95, 602 00 Brno, Czech Republic

[c]Department of Civil and Materials Engineering, University of Malaga, C/Dr Ortiz Ramos s/n, 29071 Malaga, Spain

[d]Ghent University, Faculty of Engineering and Architecture, Department of Structural Engineering and Building Materials, Valentin Vaerwyckweg 1, 9000 Ghent, Belgium.

*Corresponding Author

Petr Miarka (email: petr.miarka@vut.cz). Tel: +420 532 290 430

Abstract

In this paper, the fracture process zone (FPZ) of a high-performance concrete (HPC) is studied. The analysis is done under a pure mode II load, making use of a digital image correlation (DIC) technique. The experimental test was performed on Brazilian disc with central notch (BDCN) specimens with a relative notch ratio a/R of 0.267. The main focus of this experimental study was the traction-free crack ahead of the notch tip, together with the FPZ extent ahead of the crack. This is done by adjusting the current method for mode I crack localisation to pure mode II cracks. Additionally, a traditional analytical formulation to predict FPZ length was substituted with the fracture toughness for mode II to cover mode II load cases. To verify the adjustments to the mode I crack identification, crack tip opening (CTOD) and crack tip sliding (CTSD) displacements were measured by DIC, which showed a mode II dominance in the crack tip displacement components.

Keywords: Concrete; FPZ; Mode II; DIC.

Abbreviations/Nomenclature

3PB	three-point bending
AE	acoustic emission
BDCN	Brazilian disc with central notch
CS	coordinate system
CTOD	crack tip opening displacement
CTSD	crack tip sliding displacement
DIC	digital image correlation
EA3PB	eccentric asymmetric three-point bending
EDA	edge detection algorithm
FEM	finite element method
FOV	field of view
FPZ	fracture process zone
GBFS	granulated blast furnace slag
HPC	high-performance concrete
LEFM	linear elastic fracture mechanics
MTS	maximum tangential stress
PMMA	polymethyl-methacrylate
ROI	region of interest
SC3PB	semi-circular three-point bending
SIF	stress intensity factor
α	notch inclination angle (°)
ν	Poisson's ratio (-)
σ	stress (MPa)
γ	transformation angle (°)
σ_t	tensile strength (MPa)
a	crack length (mm)
a/R	relative crack length (-)
B	specimen's thickness (mm)

$C(y)$	horizontal displacement difference function (mm)
D	specimen's diameter (mm)
E	Young's modulus of elasticity (GPa)
f_c	compressive strength (MPa)
f_{ct}	flexural strength (MPa)
f_t	indirect tensile strength (MPa)
K_I, K_{II}	SIF for mode I, mode II (MPamm$^{1/2}$)
K_{IC}, K_{IIC}	mode I, II fracture toughness (MPam$^{1/2}$)
l_{FPZ}	FPZ length (mm)
L_{ch}	characteristic length (mm)
P	applied force (kN)
R	specimen's radius (mm)
r_C	critical distance (mm)
t	notch width (mm)
u, v	global displacements (mm)
u_1, v_1	local displacements (mm)
X, Y	global coordinate system
X_1, Y_1	local coordinate system
Y_I, Y_{II}	shape functions (-)

1. Introduction

The concrete fracture process has attracted research interest for more than six decades [1]. The progress was initially based on linear elastic fracture mechanics (LEFM) theory [2] and later on was developed as an individual research discipline in itself. Since concrete has a highly heterogenous inner structure consisting of aggregates and a cement matrix, the whole cracking process becomes a more complex mechanism for which LEFM theory appears to be a bit simplistic. Thus, multiple adjustments have been made to the LEFM to address material nonlinearity and to evaluate fracture parameters i.e. the two-parameter fracture model [3], the effective fracture model [4], the double-K model [5] as well as the connection to the size effect [6,7], which later on developed in the application on reinforced concrete structures [8,9].

This material non-linearity can be documented by a typical post-peak softening branch of the load-deformation diagram recorded during the fracture test [10–13]. The softening branch is the result of the presence of a fracture process zone (FPZ) [9] ahead of the notch tip. The presence of the FPZ during concrete cracking is the main reason for this quasi-brittle fracture behaviour after reaching the peak load. The FPZ is identified as the zone ahead of the notch tip in which multiple microcracking occurs, while traditionally the LEFM works with a single crack with its origin at its notch. Therefore, traditional methods used in fracture analysis, i.e. measuring the crack opening by strain gauge, becomes insufficient. This insufficiency has led to the employment of several advanced experimental methods, e.g., Moiré interferometry [14,15], acoustic emission (AE) [16,17], X-ray computed tomography [17–19] and digital image correlation (DIC) [20,21] or a combination of DIC and AE [22].

The FPZ is mainly associated with the tensile load produced by bending during a three-point bending (3PB) test [16,21,23], by the wedge-splitting test (WST) test [24] or recently by semi-circular three-point bending (SC3PB) test [25,26] configurations. Contrary to this, onset of failure of concrete structures is not caused by tensile crack initiation. It is often related to a combination of tension and shear damage initiation [27,28]. A typical example of such onset of failure are a simply supported reinforced beam with steel stirrups [27–29] and pre-tensioned precast hollow floor panels [30,31], which can both fail due to compressive failure of the diagonal. Other mixed-mode I/II failure mechanisms may occur for cast-in anchors [32]. However, these failure mechanisms are more complex than what is mostly studied in laboratories on smaller size specimens.

The presence of shear in a cracked concrete influences the FPZ, which tends to deflect from the straight path, as for the structure it is failure of the compressive diagonal due to indirect tension. The mixed-mode I/II fracture analysis goes hand in hand with the progress of LEFM [33,34] and resulted in the formulation of fracture criteria, which can predict such failure. The most common criteria are the maximum tangential stress (MTS) [35] and the strain energy density (SED) [36].

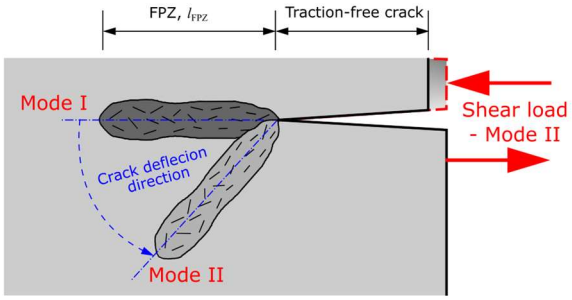

Figure 1: Influence of mode II on the shape of FPZ.

The deflection of the FPZ is due to the presence of mode II loading, which is presented schematically in Figure 1. The crack and the FPZ deflect from the expected path due to presence of mode II deformation. Several studies have dealt with the analysis of mode II failure [37,38] as well as with the FPZ under pure mode II, which is mainly done on specimens with rectangular cross-section. On the other hand, the analysis of already built structures is often done from core-drill samples, which are taken from the structure prior to renovation. Reshaping the cylinder to the rectangle increases the time, labour and cost of such tests. Thus, several studied have dealt with the analysis of the FPZ under pure mode II loading on circular specimens [39,40].

This experimental study revisits the analysis of the FPZ developed during concrete cracking, this time focusing on the analysis of FPZ development under shear mode II loading. For this, a Brazilian disc with central notch (BDCN) fracture test was coupled with the DIC method to capture the deformation produced by the external load. The displacement and strain fields allowed us for the localisation of the traction-free crack as well as for the analysis of the FPZ development in the BDCN test. The localised FPZ is expressed as strain envelope in the measured strain map. Furthermore, the obtained values of crack tip opening displacement (CTOD) and crack tip sliding displacement (CTSD) are compared to find the influence of the mode II displacement on the concrete cracking process. The ultimate goal is set to compare experimentally measured with analytically predicted FPZ lengths (l_{FPZ}).

2. Materials and Methods

In what follows, first the BDCN test specimen is introduced. Then, the concrete mixture used in this experimental study together with its measured mechanical properties are presented. Furthermore, the experimental digital image correlation (DIC) technique to capture the displacement is briefly presented together with the method used for notch tip acquisition. Additionally, an adjustment of the traction-free crack location methodology is proposed to account for the mode II load condition. Lastly, a review of current analytical formulas used for prediction of the FPZ size is presented and discussed. This provides a solid base for a comprehensive analysis of this challenging problem.

2.1 Brazilian Disc with Central Notch (BDCN)

In this study, a BDCN specimen was selected due to the relatively simple specimen preparation and experimental testing, but also due to the presence of pure mode II. The BDCN specimen was made from a standardized cylinder, which was cut using a diamond saw to the required thickness [41]. The initial notch was introduced by a water jet cutter to produce a straight notch. The dimensions of the BDCN specimen are of diameter D = 149.21 mm, thickness B = 31.5 mm with an initial notch length $2a$ of 40 mm. The BDCN specimen's dimensions and its boundary conditions are presented in Figure 2(a).

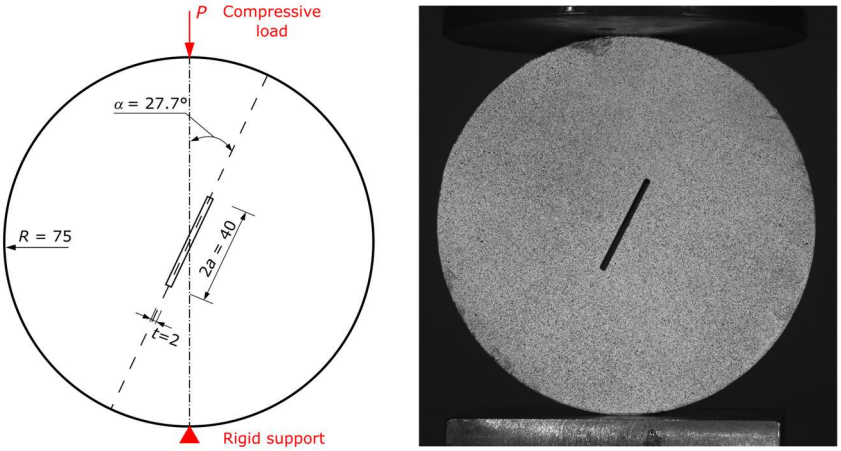

(a) (b)

Figure 2: Dimensions and boundary conditions of BDCN - (a) and (b) - BDCN specimen with applied speckle pattern..

Prior to the experimental test, a speckle pattern was applied on the surface of the BDCN specimens. This speckle pattern consists of black and white speckles with a random grey intensity distribution, which allow a proper data acquisition since the concrete has relatively large aggregates, which are not suitable for DIC measurements without speckle pattern.

The equipment for the static fracture tests is a MTS servo-hydraulic rig with a maximum capacity of 100 kN and a speed 0.01 mm/s. This test machine is accompanied by a Flir Gazelle CCD camera with a resolution of 4.1 MPx and 150 FPS combined with a Schneider lens together with two light sources to ensure good homogeneous light conditions for correct DIC technique measurements. Such a camera organization provides a field of view (FOV) of 181.24 × 181.24 mm^2. To reduce misaligned error, the working distance was increased, setting a distance of 80 cm. Because of the quick failure in the material, 15 pictures were taken each second. The digital images are processed by VIC 2D V6 software in order to obtain a displacement field [42]. A similar test set-up was used in a previous study [43].

To analyse the fracture behaviour and FPZ size, the stress intensity factors (SIF) values are calculated using Eq. (1):

$$K_i = \frac{P\sqrt{a}}{RB\sqrt{\pi}} \frac{1}{\sqrt{1-\frac{a}{R}}} Y_i(a/R, \alpha), \tag{1}$$

where i is the crack opening mode I or II, P is the applied compressive load, R is the specimen's radius, a is the crack length, α is the notch inclination angle, B is the thickness of the specimen and Y_i are the shape functions for mode I and mode II, respectively.

The shape functions for mode I and mode II can be found in literature, e.g. in the handbook by Tada & Paris [44] or in a paper by Seitl et al. [45]. The effect of distributed load on the values of geometry shape functions and consequent fracture toughness can be found in studies by Tang [46,47]. The specimen was tested under a pure mode II load, which is achieved for a relative notch ratio a/R = 0.267 by an angle α = 27°. In that case, the values of the shape functions are Y_I = 0 for mode I and Y_{II} = 1.55 for mode II. The fracture toughness for mode I K_{IC} and for mode II K_{IIC} are calculated using the maximum measured force obtained in the test. In this experimental study, values of fracture toughness K_{IC} and K_{IIC} were used form previous study performed on the exact same mixture by Miarka et. al. [48].

2.2 Mixture Composition

The studied HPC mixture uses Portland cement CEM I 42.5 R as a binder together with three admixtures: metakaolin, GBFS and limestone. Natural sand 0/4 mm and crushed high quality granite 4/8 mm are used as aggregates. The mixture was mixed in small volume batches of 0.7 m^3 and poured directly into

the moulds. The material composition is equal to that used in previous work [43,48]. The mixture's composition per m^3 is shown in Table 1.

Table 1: Material composition of the studied HPC per m^3.

	CEM I 42.5R	GBFS	Limestone	Metakaolin Metaver	Superplasticizer (Glenium 300)	Water	Sand 0/4	Crushed aggregates 4/8
[kg]	650	60	15	75	17	165	400	600

At the age of 28 days, the mechanical properties of this HPC mixture were measured in accordance with European standards and are presented in Table 2.

Table 2: Mechanical parameters (mean values with their standard deviations) of the studied HPC at 28 days.

Compressive strength $f_{c,cube}$ [MPa]	106.2 ± 2.5
Young's modulus E [GPa]	41.0 ± 0.6
Flexural strength $f_{c,t}$ [MPa]	9.3 ± 0.9
Indirect tensile strength f_t [MPa]	6.43 ± 0.3

This mixture was previously tested to analyse its fracture mechanical properties using BDCN specimens resulting in a fracture toughness for mode I K_{IC} of 34.93 MPamm$^{1/2}$ and for mode II K_{IIC} of 52.04 MPamm$^{1/2}$, see [43,48].

2.3 DIC Data Extraction

DIC was used to investigate the crack tip behaviour of the BDCN specimen under mode II. DIC provides full-field displacement information by comparing images taken before and after straining the specimen body [49]. Each image is divided into smaller regions, or 'interrogation windows'. Based on the speckle pattern, a subset of 29×29 pixels was defined with an overlap between subsets of 7 pixels. The cross-correlation product [50] is used to measure the similarity between the interrogation windows before and after straining the body for the purposes of the study:

$$c'(u,v) = \frac{\sum_{x=-\frac{N}{2}}^{y=\frac{N}{2}} \sum_{x=-\frac{N}{2}}^{y=\frac{N}{2}} I_A(x,y) I_B(x+u, y+v)}{\sqrt{\sum_{x=-\frac{N}{2}}^{y=\frac{N}{2}} \sum_{x=-\frac{N}{2}}^{y=\frac{N}{2}} I_1^2(x,y) \sum_{x=-\frac{N}{2}}^{y=\frac{N}{2}} \sum_{x=-\frac{N}{2}}^{y=\frac{N}{2}} I_2^2(x+u, y+v)}} \quad (2)$$

where *c'* is the normalised cross-correlation product, which is a function of u and v, these being the displacement vectors joining the centres of the two regions of interest along directions x and y, respectively. I_A and I_B are the intensity distributions of the two digital images before and after straining the sample, respectively, and N is the number of interrogation windows into which the digital images were divided. The maximum value of the normalised cross-correlation product (Eq. (2)) is the probable displacement vector for the centre of each interrogation window in I_A.

The notch tip position was determined by Sobel's edge detection algorithm (EDA) as implemented in the MATLAB image processing toolbox [51]. Sobel routine often finds application in image processing analyses. It searches for regions with significant discontinuities within a 2D displacement map. It assigns a value of 1 to the regions with a significant discontinuity, and a value of 0 elsewhere. The edge, in this case the notch, is located along the region with a value of 1. The crack/notch is identified along the points where an edge is detected with a notch tip located at the end of the identified edge.

Typical horizontal displacement fields u and vertical displacements fields v with marked notch tip locations prior the onset of cracking together with a detail on the notch tip with Sobel's points are shown in Figure 3.

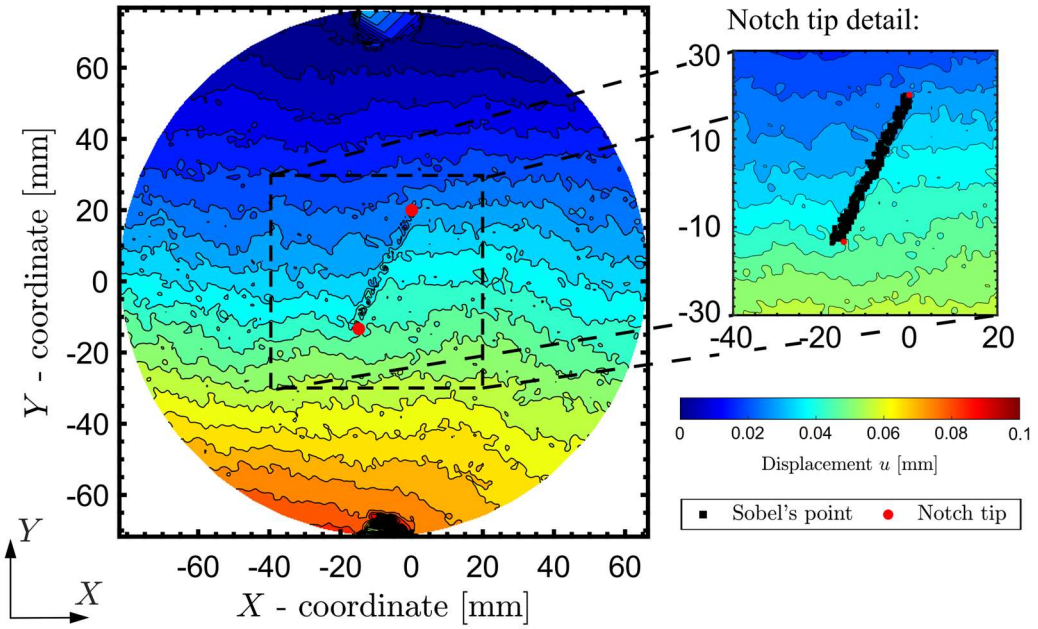

(a)

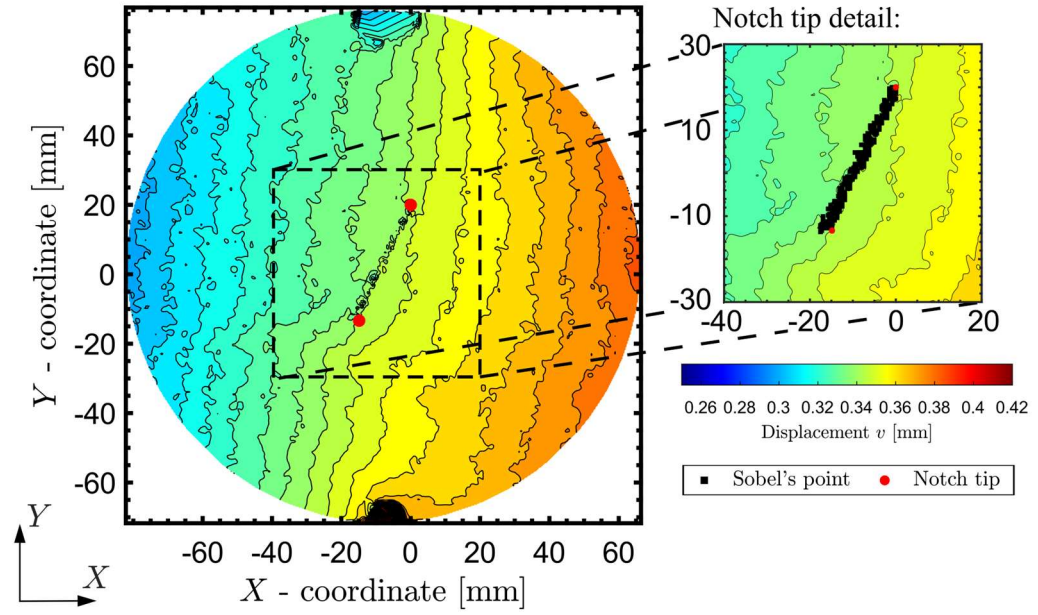

(b)

Figure 3: Captured displacement fields by DIC technique together with a detail on the notch tip location as obtained from Sobel's search algorithm - (a) - horizontal displacement *u* and (b) - vertical displacement *v*.

The slight asymmetry observed in Figure 3 in both displacement maps indicates the presence of mode II deformation induced by notch inclination. Such a mode II deformation plays a key role in the onset of fracture and has a major influence on the crack initiation direction. Other discontinuities generated by the induced load can be observed at the bottom and the top of the disc in Figure 3(a) and Figure 3(b), which have to be omitted in further analysis as they provide misleading information. Therefore, in the further DIC analysis, we reduce the region of interest (ROI) of the DIC displacement fields to a location around the notch tip with a dimension of 40×60 mm^2. This ROI excludes the high compressive strain concentrations located at the bottom and the top of the disc (as observed in Figure 3) and allows analysing each crack/FPZ separately, as the crack detection algorithm might sometimes provide misleading results. [52].

Although the MATLAB image processing toolbox offers various EDAs e.g., the Canny method [53] is using the Gaussian filter, and hence being more insensitive to noise. However, the Canny method uses two parameters as an input (threshold and standard deviation σ). To demonstrate differences in the detected notch tip locations, a comparison of the edge detection results with different initial settings at $P = P_{max}$ is given in Figure 4 for the horizontal displacement field u and in Figure 5 for vertical displacement field v.

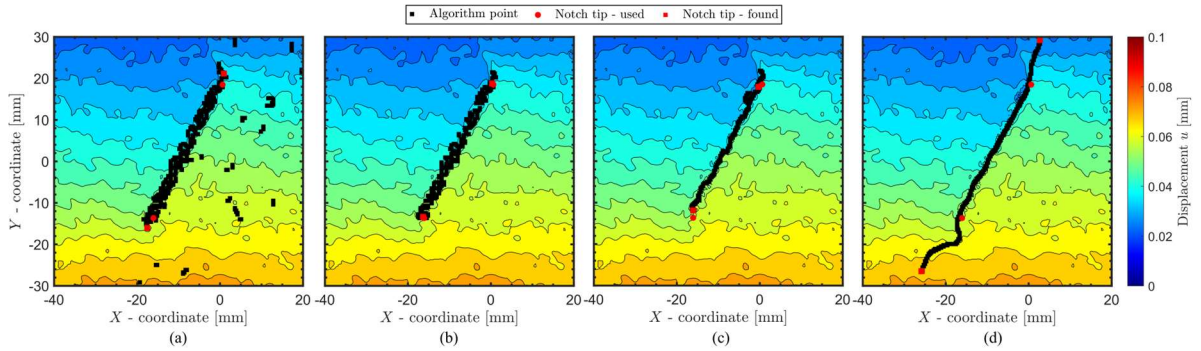

Figure 4: Comparison of edge detection algorithm with different initial settings visualised in horizontal displacement field u at $P = P_{max}$ – (a) Sobel algorithm with threshold of 1×10^{-3}, (b) – Sobel algorithm with threshold of 2×10^{-3}, (c) – Canny algorithm with threshold of 1×10^{-1} and $\sigma = 1.4$ and (d) – Canny algorithm with threshold of 1×10^{-1} and $\sigma = 5$.

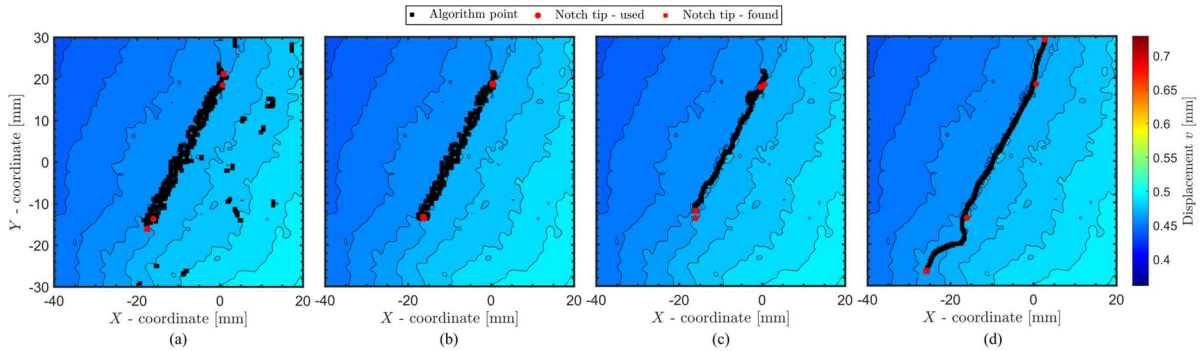

Figure 5: Comparison of edge detection algorithm with different initial settings visualised in vertical displacement field v at $P = P_{max}$ – (a) Sobel algorithm with threshold of 1×10^{-3}, (b) – Sobel algorithm with threshold of 2×10^{-3}, (c) – Canny algorithm with threshold of 1×10^{-1} and $\sigma = 1.4$ and (d) – Canny algorithm with threshold of 1×10^{-1} and $\sigma = 5$.

A clear difference in the edges detected using different algorithms with different initial settings can be observed in Figure 4 and Figure 5. The edge locations generated by the Sobel algorithm show the correct notch length with the correct thickness for both threshold values (see Figure 4(a)-(b) and Figure 5(a)-(b)). The lower value of threshold i.e., 1×10^{-3} found discontinuities outside of the notch tip region, while the higher threshold of 2×10^{-3} limit found the discontinuities in the correct notch tip region.

On the other hand, notch tip locations found by the Canny algorithm, as presented in Figure 4(c)-(d) and Figure 5(c)-(d), show a thinner notch width for both initial algorithm settings. Furthermore, the highest difference in the detected notch tip position can be observed for the setting with a threshold of 1×10^{-1} and σ of 5 (see Figure 4(d) and Figure 5(d)), where the results showed the notch length to be nearly 60 mm. This can be related to the fact that the edge detection procedure was performed at the maximum load P_{max} with a crack already present in the BDCN specimen.

Since the Sobel algorithm is a single parameter method and the authors have a long experience using it, it will be used in further analysis with a threshold set to 2×10^{-3}. This approach was previously used also in fatigue and fracture applications [54,55]. An interesting comparison of different methods for locating the crack tip from DIC maps [56] is also available. Most of the DIC studies performed on concrete are not searching for the notch/crack tip location and rather directly analyse the displacement fields (see [21,40,57–59]). A similar method was previously used on concrete specimens with reliable results [43].

Thus, the use of the edge detection method applied on concrete represents unique procedure in the DIC analysis that significantly improves post-processing of the experimental results. ~~To the authors' knowledge, this is the first time that such a procedure has been applied to concrete.~~

The observed results from the notch tip localisation methods and their initial settings are compared with the used notch tip location in further analysis. The comparison is given in Table 3 together with the calculated absolute and relative differences in the localised X and Y coordinates.

Table 3: Comparison of detected notch tip locations by various algorithms using different initial settings.

			Top notch		**Bottom notch**	
	Localised notch tip at:		X [mm]	Y [mm]	X [mm]	Y [mm]
			0.62	18.49	-16.06	-13.66
Algorithm: Sobel	Threshold: 1×10^{-3}	Location [mm]	0.91	21.17	-17.55	-16.04
		Abs. diff [mm]	-0.29	-2.68	1.49	2.38
		Rel. diff [%]	48 %	14 %	2.4 %	17 %
	Threshold: 2×10^{-3}	Location [mm]	0.32	18.79	-16.36	-13.36
		Abs. diff [mm]	0.30	-0.3	0.3	-0.30
		Rel. diff [%]	48 %	1.6 %	1.85 %	2.2%
Algorithm: Canny	Threshold: 1×10^{-1} $\sigma = 1.4$	Location [mm]	-0.28	17.90	-16.06	-11.88
		Abs. diff [mm]	0.89	0.60	0.0	-1.79
		Rel. diff [%]	145 %	3.2 %	0 %	13 %
	Threshold: 1×10^{-1} $\sigma = 5$	Location [mm]	2.70	29.21	-25.86	-26.46
		Abs. diff [mm]	-2.08	-1.72	9.80	12.80
		Rel. diff [%]	339%	58 %	61 %	93 %

From Table 3 a clear difference can be observed in the obtained notch tip locations depending on the chosen algorithm. Sobel algorithm with a threshold of 1×10^{-3} detects the Y-coordinate of the notch tip with an error limited to 14% and 17% for the top and bottom notch, respectively, while for the threshold of 2×10^{-3} this reduces to 1.8% and 2.2%, respectively. The X-coordinate shows an error of 48% for the top notch locations for both threshold values, while the bottom notch has an error limited to 2.4%. The results generated by the Canny algorithm confirm the observation made Figure 4 and Figure 5 with the high inaccuracy of the detected notch tips. Furthermore, the Canny algorithm with threshold of 1×10^{-3} and $\sigma = 1.4$ detects the notch tip locations more accurately than the settings with a threshold of 1×10^{-3} and $\sigma = 5$ for both notch tips. The miss-detection in X-coordinate can be manually adjusted with insignificant influence in the further FPZ analysis, while the correct Y-coordinate of the notch tip plays a crucial role in the FPZ analysis as its length is one of the main results.

Given the non-invasive and relative simplicity of the DIC technique, the current approach (Sobel algorithm) could be adapted to be used on real concrete structures, and not just on laboratory environments. From an industrial application point of view, Sobel EDA appears to be better suited than Canny EDA, since it requires less input from the user.

2.4 Identification of a Traction-free Fracture Crack Tip

Chen et al. in [57] proposed a methodology to identify the transition point between the traction-free crack and the FPZ. Such a methodology uses the horizontal displacement difference function C, which varies over the y-coordinates. The function $C(y)$ is obtained from the horizontal displacements $u(y)$ along two parallel lines along the crack. These two parallel lines are in equidistant distance δ from the crack/notch. The traction-free fracture can be found when $C(y) \approx 0$ and $\partial C(y)/\partial y \approx 0$. The FPZ is then located above this point. The traction-free crack identification process is schematically shown in Figure 6(a).

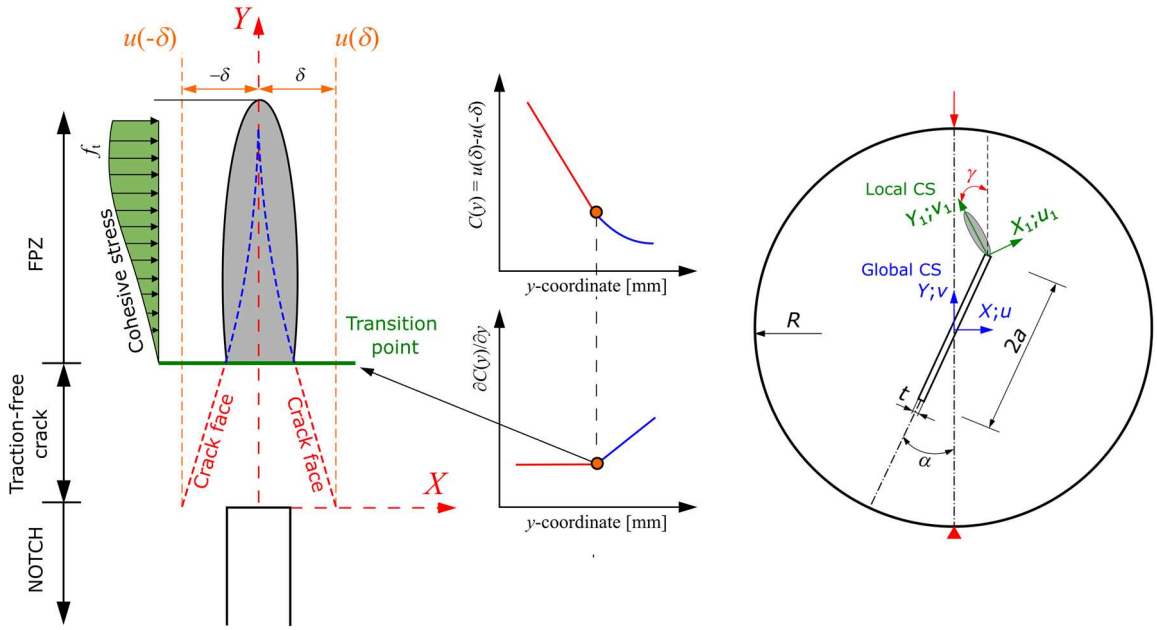

Figure 6: Traction-free crack tip localization for mode I crack (a) and (b) - transformation of a crack tip displacements to a local coordinate system X_1-Y_1.

Unfortunately, this methodology initially proposed by Chen [57] is only valid for tensile mode I cracks. Thus, we decided to adopt this methodology and upgrade it to pure mode II load conditions. Since the crack, which is exposed to mode II load, will deflect from the straight path towards the loading point as assumed in Figure 1, it is necessary to distinguish between mode I and mode II displacements. This leads to a transformation from the global coordinate system (CS) X-Y to a local CS X_1-Y_1. The new CS X_1-Y_1 has its origin at the notch tip with the Y_1 axis parallel to the crack. This transformation provides crack opening displacements u_1 and crack sliding displacements v_1. The transformation angle γ has in this case a counter clockwise direction. The transformation from the global X-Y to the local X_1-Y_1 CS is shown in Figure 6(b). These two coordinate systems are linearly transformed, thus the displacements gradients are also linearly related [40]. The new coordinate system allows the determination of both displacements parallel and perpendicular to the crack, unlike the initial coordinate system where displacements were measured parallel and perpendicular to the load, independently on the crack angle. Therefore, the methodology mentioned above is also valid for mixed-mode I/II load conditions.

The traction-free crack identification methodology proposed by Chen as presented in Figure 6(a) is then carried out in the local CS X_1-Y_1 with the use of the horizontal displacements $u_1(y)$ along two parallel lines to the crack to locate the traction-free crack. The horizontal displacement difference function in the local coordinate system X_1-Y_1 follows the same conditions for the traction-free crack tip identification i.e. $C(y_1) \approx 0$ and $\partial C(y_1)/\partial y_1 \approx 0$. Such proposed adjustments for mixed-mode I/II cracks are highly dependent on the origin of these equidistant lines as well as on the transformation angle γ. The origin of these lines should be placed inside of the FPZ and simultaneously outside from the notch tip location to be able to correctly capture functions $C(y)$ and $C(y_1)$. Such arrangement reduces error caused by the concrete heterogenous microstructure.

Although the BDCN specimen is loaded under pure mode II load due to geometrical conditions, further crack propagation and fracture of the specimen are due to mode I i.e., crack opening mode. The same assumption is used in traditional and recent fracture criteria for mixed-mode I/II fracture assessment.

2.5 Estimation of FPZ Size

The critical distance r_C is a material parameter which expresses the distance from the notch tip in which the crack opening stress exceeds the material's yielding stress or for concrete the tensile strength. The

critical distance was originally derived to represent the plastic zone length ahead of crack tip of elastic-plastic material such as metals and was introduced by Irwin [60] as:

$$r_C = \frac{1}{2\pi}\left(\frac{K_{IC}}{\sigma_t}\right)^2 \text{ – plane stress,} \tag{3}$$

$$r_C = \frac{1}{6\pi}\left(\frac{K_{IC}}{\sigma_t}\right)^2 \text{ – plane strain.} \tag{4}$$

where σ_t is the tensile strength.

The original plastic zone length as derived by Irwin has been adopted for concrete materials for which it is often referred to as the characteristic length L_{ch} and it is proportional to the size of the FPZ. Hillerborg et al. [10] formulated the characteristic length L_{ch} by using a fictious crack model as:

$$L_{ch} = \left(\frac{K_{IC}}{\sigma_t}\right)^2. \tag{5}$$

These above-mentioned formulas for the estimation of the FPZ size use the mode I fracture toughness K_{IC}. Recently, Aminzadeh et. al [61] analysed a PMMA material under pure mode II load conditions using the mode II fracture toughness K_{IIC} as a substitution for the mode I fracture toughness K_{IC} in the classical Irwin formulation for the critical distance r_C. This study showed good agreement between analytical predictions and experimental values for the polymethyl-methacrylate (PMMA) material.

In addition to these formulas, Bažant [62] and Otsuka [63]linked the FPZ of the concrete to directly to the size of the maximum aggregate d_{agg} used in the mixture. This connection was recently studied by Alanazi & Susmel in [64] for both static and cyclic loads unveiling a good prediction of the failure of the specimen.

A comparison of FPZ sizes estimated using Eqs. (3)-(5) together with measured material properties for both mode I and mode II load cases is given in Table 4.

Table 4: Estimation of FPZ length based on different analytical and empirical approaches.

	Fracture toughness [MPamm$^{1/2}$]	Tensile strength f_t [MPa]	r_C [mm] - plane stress (Eq. 3)	r_C [mm] - plane strain (Eq. 4)	L_{ch} [mm] - (Eq. 5)	d_{agg} [mm]
Mode I	34.93	6.30	4.89	1.63	30.74	8
Mode II	52.04	6.30	10.76	3.61	68.22	8

The obtained values of critical distances r_C and characteristic lenghs L_{ch} as presented Table 4 agree with the general expectation, i.e. the predicted FPZ length is longer for mode II as the K_{IIC} value is approx. 1.5 times higher than the value of K_{IC}.

Another method used for the prediction of the FPZ size was proposed by Jianhong [65], which is based on the critical tensile strain $\varepsilon_{xx,C}$ produced by the load prior to the specimen's failure. The critical strain $\varepsilon_{xx,C}$ can be calculated as

$$\varepsilon_{xx,C} = \frac{\sigma_t}{E_t} = \frac{\sigma_t}{(0.72E_c)}. \tag{6}$$

where E_t is the tensile modulus and E_c is the compressive modulus. Eq. (6) is based on measurements performed on rocks and the reduction of compressive modulus E_c by 28% was proposed by Chen [57] without further clarification. Although this empirical formulation for the specimen's failure is based on rocks, it can provide valuable information on the material's failure under pure mode II, since all other analytical formulas, i.e. Eqs. (3)-(5), use the fracture toughness for mode I. The calculated value of the critical strain $\varepsilon_{xx,C}$ is approx. 2×10^{-4}, which will serve as an envelope in the DIC strain map around the traction-free crack tip.

3. Results and Discussion

In this section, we give a comprehensive overview of the experimentally obtained results. We begin with the presentation of the FPZ evolution during the BDCN test under pure mode II load conditions. Afterwards, we show the DIC data with the location of the traction-free crack together with the FPZ extent ahead of it. Finally, we provide an overview of measured FPZ length properties and discuss the obtained values of crack opening and crack sliding displacement components.

3.1 FPZ Evolution under Pure Mode II

Since the focus of this paper is to analyse the FPZ under pure mode II loading conditions, the evolution of the FPZ during the test is presented. The load-displacement *P-d* diagram of a BDCN specimen shows a linear elastic behaviour up to 60% of the maximum applied load. After reaching this value, a crack starts to propagate, as well as the FPZ. Only after reaching this point the DIC measurement begins with the intent to reduce the amount of processed data. For the BDCN geometry, the crack and the consequent FPZ start to localise at both notch ends, which provides twice as much information as for a 3PB specimen. The FPZ evolution for different applied load ratios P/P_{max} is presented in Figure 7.

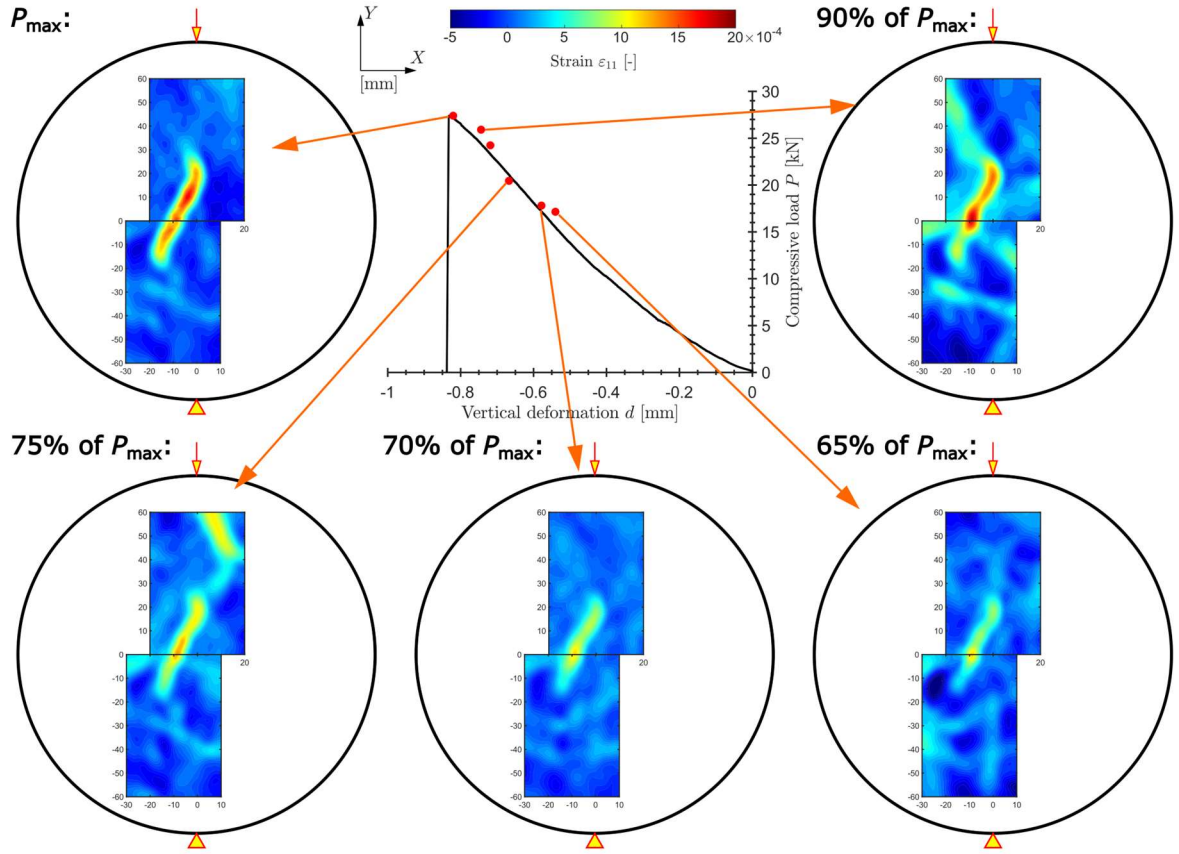

Figure 7: Development of principal strain ε_{11} and localization of the FPZ under pure mode II load ($a/R = 0.267$ $\alpha = 27°$).

An inclination/shift of the FPZ from the vertical path with a direction to the loading point can be observed in Figure 7, which follows the general expectation presented in Figure 1. The FPZ increases in size with the increasing load, which again follows the assumptions made earlier in this paper. Moreover, the inclination of the FPZ is related to mode II load presence, which plays a key role in the crack initiation process. Another interesting property observed in Figure 7 is the asymmetric propagation of the FPZ from both notch ends. This observation is in contradiction with the assumption stated above.

Nonetheless, concrete is a highly heterogenic material with aggregates of size up to 8 mm. This may eventually manifest itself as a crack arrest due to the presence of a coarse aggregate ahead of the crack tip. Additionally, this may lead to a temporary increase in the load capacity, as the crack has to overcome

a longer/greater distance around the aggregate. Afterwards, the crack can propagate at a higher speed due to the accumulated energy in the specimen, which manifests itself in a typical splitting behaviour of the test.

3.2 Traction-free Crack and FPZ Extension

To illustrate the methodology for localisation of the traction-free crack under pure mode II, the DIC analysis was performed for the maximum load induced to the BDCN specimen. For simplicity reasons, we show in more detail the displacements and strains obtained for the ROI located at the top notch. However, the same methodology was used for ROI placed at the bottom notch.

To localise the traction-free crack, two lines were selected on the left and right side with a distance δ = 2.5 mm from the centre of the notch (the distance between them is 2δ = 5 mm). Then these lines were inclined by an angle γ = 18°, which serves as a transformation angle from the global CS X-Y to the local CS X_1-Y_1. Afterwards, the horizontal displacement u_1 is extracted from both of these lines, and consequently, the displacement difference function $C(y_1)$ can be assembled. This process of localization of the traction-free crack together with its location is illustrated in Figure 8.

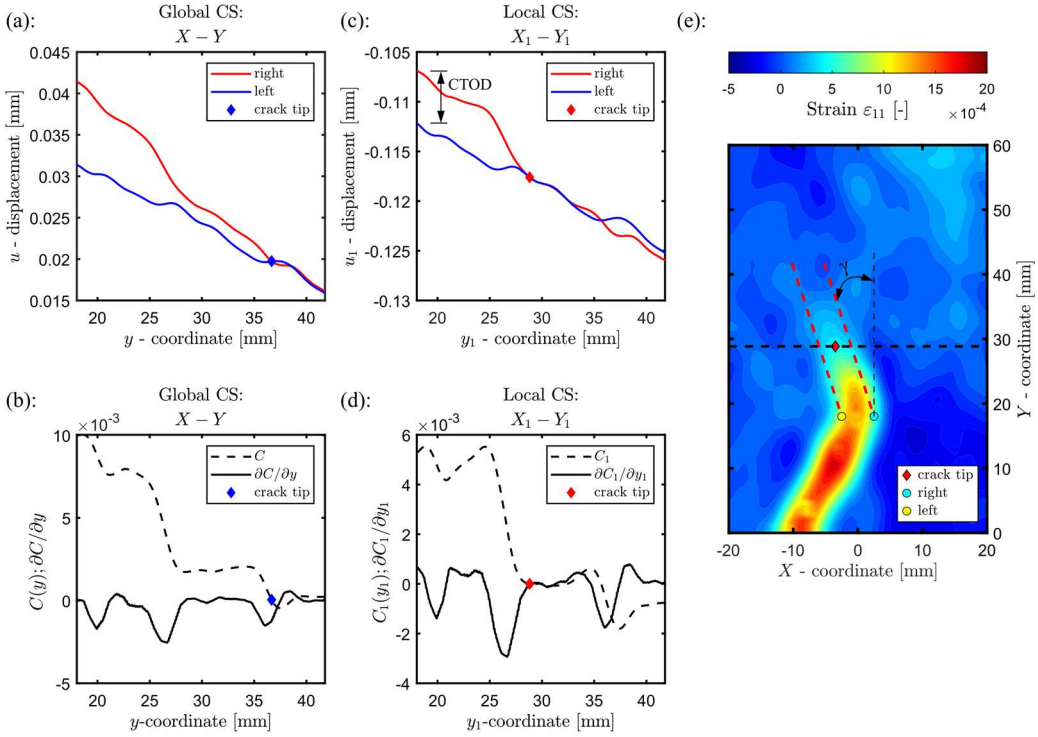

Figure 8: Traction-free crack localisation process under pure mode II load (a) - displacement u in the global CS X-Y, (b) - function $C(y)$ and its derivation $\partial C(y)/\partial y$ in the global CS X-Y, (c) - displacement u_1 in the local CS X_1-Y_1, (d) - function $C(y_1)$ and its derivation $\partial C(y_1)/\partial y_1$ in the local CS X_1-Y_1 and (e) - location of the traction free crack in ε_{11} strain map.

In Figure 8 a clear difference can be observed in the displacements in the global X-Y (Figure 8(a-b)) and in the local X_1-Y_1 (Figure 8(c-d)) CS. Moreover, if the displacements in the global CS X-Y are used for pure mode II cracks, a clear overestimation of the traction-free crack length can be observed. This difference in the crack length is due to the presence of mode II displacements v acting in the direction of the global X-axis, while in the case of the local CS mode I and mode II displacement can be separated and eventually CTOD and CTSD can be obtained to determinate the role of each displacement component in cracking process. Even though CTOD is often used as a fracture parameter, the use of CTSD as an additional parameter has now been proven to be very convenient to complement the crack tip information [66,67].

The two equidistant lines used for the traction-free crack identification, the obtained location of traction-free crack, the location of the two points used for the extraction of the CTOD and CTSD values are

shown in Figure 8(e) in a principal strain ε_{11} map. Such a plot of the obtained results demonstrates the extent of the FPZ ahead of the traction-free zone, which in this case is larger than the traction-free crack.

Since the methodology used for the traction-free crack identification depends on the distance δ from the centre of the notch tip and on the transformation angle γ, a brief parametric study that vary these two-parameters was performed. In the Case I, the distance 2δ varies from 2 to 10 mm with the notch tip placed in the centre of these lines (distance δ is the same to left and right points), while in the Case II the distance 2δ was set to 5 mm with varying transformation angle γ from an interval of <10° - 30°>. The results of this parametric study and a schematic overview of the varied parameters are presented in Figure 9.

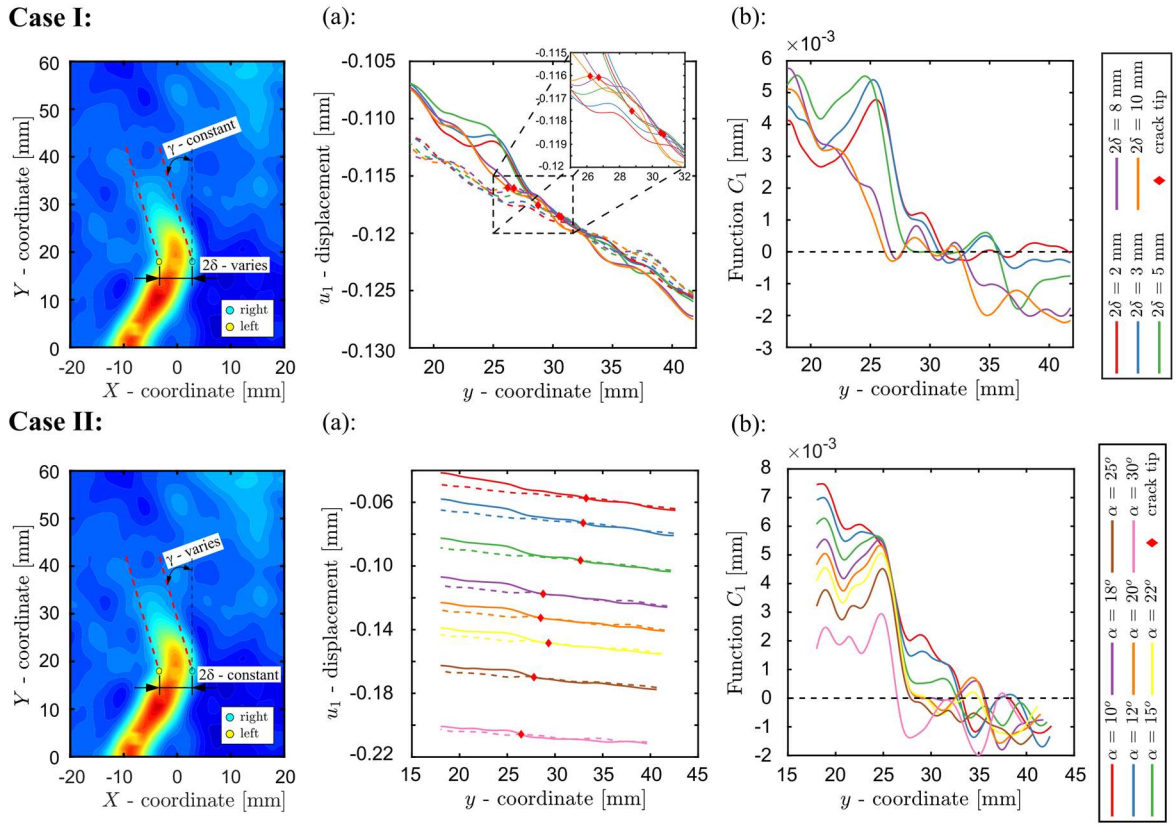

Figure 9: Results of the parametric study: Case I(a) – obtained u_1 displacements from the selected lines dependent on the distance 2δ and (b) – obtained displacement difference function C_1, Case II(a) – obtained u_1 displacements from the selected lines dependent on the angle γ and (b) – obtained displacement difference function C_1.

Figure 9 presents results of the parametric study performed as a difference in the obtained locations of traction-free crack. An interesting observation of Case I can be made in which, the obtained crack tip locations for the distance $2\delta = 5$ mm can be interpreted as a mean value with a variation of 2 mm for other distances. The results obtained by the smaller distance 2δ of 2 and 3 mm are influenced by the displacement field discontinuity produced by the crack Furthermore, the notch tip locations for the higher values of the distance $2\delta = 8$ and 10 mm are located outside of this region with the discontinuity in the measured displacement field. On the other hand, Case II shows crack tip locations according to general expectations, i.e., the crack tip location is moving with a changing transformation angle γ. The results of obtained traction-free crack tip locations from Case I are presented in Table 5, while the results for Case II are shown in Table 6.

Table 5: Comparison of obtained traction-free crack tip locations dependent on the distance 2δ.

Distance	2δ [mm]	2	3	5	8	10
Traction-free crack coordinates	X [mm]	-0.119	-0.119	-0.118	-0.116	-0.116
	Y [mm]	30.51	30.70	28.76	26.73	26.20

The observations made from Figure 9 are supported by the crack tip locations presented in Table 5, in which the X-coordinate has a similar value for all the studied distances 2δ, while the Y-coordinates are changing with different distance 2δ. The values of Y-coordinates vary by 2 mm from the selected value $2\delta = 5$ mm.

Table 6: Comparison of obtained traction-free crack tip locations dependent on the transformation angle γ.

Transformation angle	γ [°]	10	12	15	18	20	22	25	30
Traction-free crack coordinates	X [mm]	-0.057	-0.073	-0.073	-0.118	-0.133	-0.149	-0.170	-0.206
	Y [mm]	33.26	32.95	32.95	28.76	28.50	29.32	27.79	26.45

The variation of transformation angle γ, as presented in Table 6, changes the X and Y-coordinates of the crack tip found according to the general expectation. In Table 6, it can be again observed that the Y-coordinate values obtained with angles $\gamma = 18$ and 20° differs by 0.16 mm. This is a marginal difference given the high heterogeneity of concrete with aggregate size d_{agg} of 8 mm. Finally, using this approach of two parallel lines one can reduce the error of the incorrect notch tip identification by the EDA as the centre of the notch tip is situated in between the lines used for the displacement extraction.

This effect of overestimation of the traction-free crack and FPZ size can be illustrated using the strain maps captured by the DIC technique. For strains, this effect can be seen for the strains in the direction of the global X-axis ε_{xx} and for the principal strains ε_{11}. The comparison of ε_{xx} with principal strains ε_{11} is presented in Figure 10.

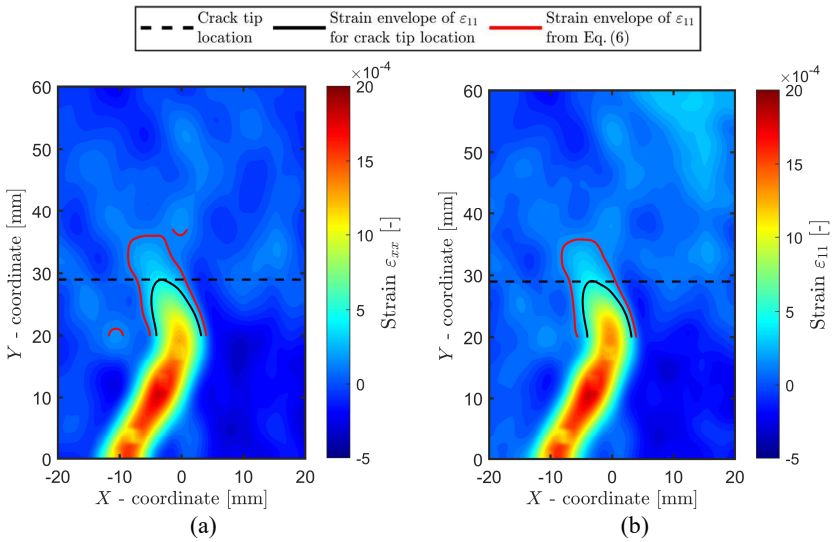

Figure 10: Comparison of measured DIC strains for maximum load – (a) ε_{xx} and (b) ε_{11} together with the traction-free crack and FPZ extend.

Careful observation of Figure 10(b) shows a minor change in the measured strain ε_{11} map located on the top right, around coordinates (x = 15 and y = 55). This is the location where the load is applied to the BDCN specimen, which often leads to stress concentrations and consequently introduces as a secondary crack development for the maximum load P_{max}. Nonetheless, these possible high stress concentrations and strain localisations do not affect the strains in the vicinity of the notch tip. The principal strains ε_{11} as presented in Figure 10(b), show generally lower values ahead of the traction-free crack tip, which extend to a wider region towards the loading point. The measured strain maps of ε_{xx} show similar values of strain as for the FPZ at a further distance from the traction-free crack. This difference is again due to the action of vertical deformations, which is not considered in the ε_{xx} strains. Thus, for further analysis, principal strains ε_{11}will be used.

Besides the strain maps of ε_{11}, a traction-free crack can be observed in the captured displacement field u. To illustrate the traction-free crack ahead of the notch, the change of the horizontal displacements

$u(x)$ along the X-coordinate can be extracted from various vertical positions i.e. different Y-coordinates. The captured horizontal displacement u map together with the location of the $u(x)$ extraction lines are shown in Figure 11(a) for the top notch position, while the displacement $u(x)$ development for various vertical locations is shown in Figure 11(b).

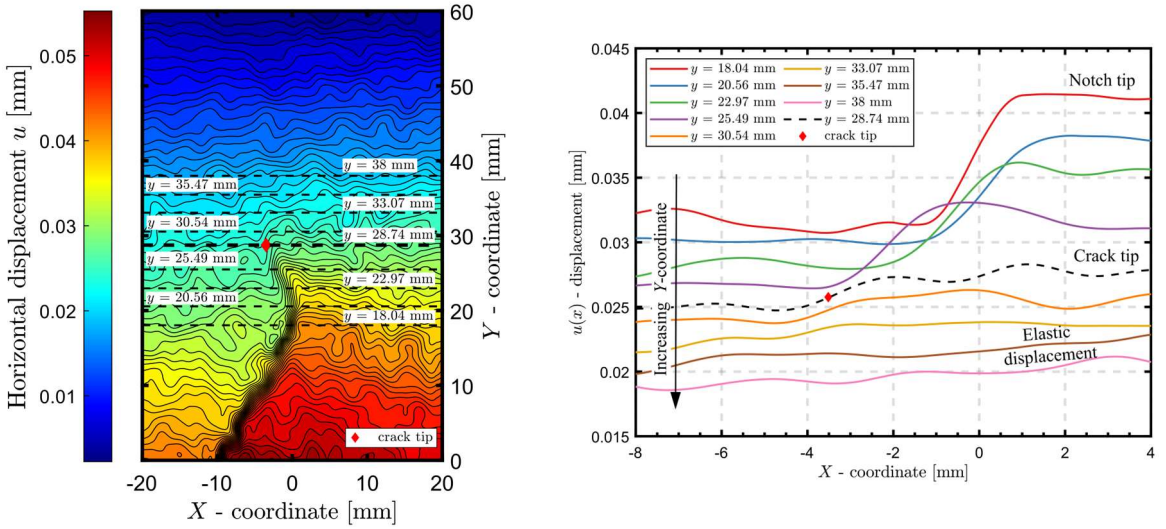

Figure 11: Traction-free crack location showed in captured horizontal displacement u map - (a) and (b) - the development of the horizontal displacement $u(x)$ for a different vertical (Y-coordinates) locations.

Figure 11(a) shows an illustrative horizontal displacement u map with a typical discontinuity located ahead of the notch tip. This discontinuity can be observed more clearly in Figure 11(b), where it is represented as a rapid increase in the displacement value $u(x)$. This discontinuity decreases with increasing Y-coordinate as the crack and consequent FPZ did not fully progress through the specimen's ligament ahead of the notch tip. Additionally, Figure 11(b) shows important positions of the horizontal displacement u fields, which are typical for a displacement field with a crack, i.e., notch tip, traction-free crack, and a typical evolution of the elastic displacement u, which is present above of the FPZ in the uncracked material.

The FPZ extent ahead of the crack tip is presented as a principal strain ε_{11} envelope for the value estimated by using Eq.(6) - approx. 2×10^{-4}. Localised traction-free cracks for maximum induced load P_{max} and with the extent of FPZ for the top notch region are presented in Figure 12(a), while the bottom region is shown in Figure 12(b).

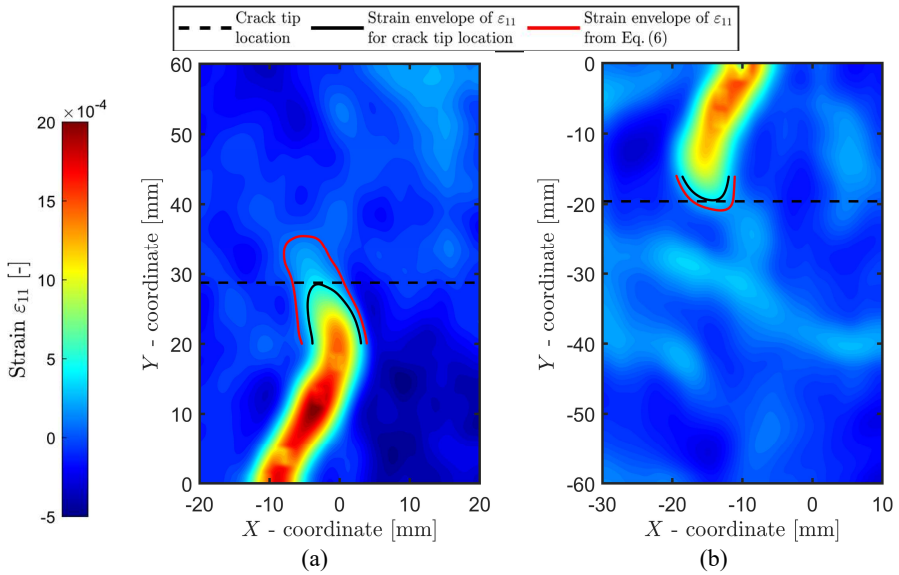

Figure 12: Comparison of DIC measured ε_{11} strains measured for maximum load with the traction-free crack location for a/R = 0.267 α = 27° – (a) top notch and (b) bottom notch.

From Figure 12 an earlier observed asymmetry in Figure 7 of the FPZ development can be seen more in detail. Figure 12(a), i.e, top notch, indicates the initiation of the crack branching ahead of the localised FPZ as well as the initiation of a secondary crack from the location of the loading point (see the top right hand side corner). The bottom notch as presented in Figure 12(b) indicates crack branching with a longer strain map intensity located around the notch tip. The localisation of the secondary crack with origin at the bottom of the disc (rigid support) can also be distinguished here. The FPZ located at the bottom notch shows a smaller length if compared to the FPZ located at the top notch. This FPZ retardation observed for the bottom notch and the crack branching can be related to the presence of a coarse aggregate ahead of the traction-free crack/FPZ, which results in a lower FPZ length as it is believed than aggregates exhibit a better mechanical performance(tensile strenght) compared to the surroung cement matrix.

Another reason for the reduction of the FPZ size can be the shear interlocking of the aggregates in the cracked material, which leads to a smaller vertical deformation and to a reduction of the transverse displacement acting in the crack opening direction. This is similar to the wedging effect observed in very tortuous cracks [55,68,69]. Lastly, this difference in the size of the FPZ can be caused by a lower induced vertical displacement while keeping the maximum value of the load, when the picture for the DIC was taken.

3.3 FPZ Properties

Since the DIC strain maps show different sizes of the FPZ for both notch ends, it is important to analyse the crack opening and sliding to verify these statements. Thus, the measured values of the CTOD and the CTSD ~~displacement components~~ were extracted from the notch tips as presented in Figure 8(e). Both CTOD and CTSD were obtained as a difference in displacements u_1 and v_1, i.e., the displacement in the local CS X_1-Y_1. The determined values of CTOD and CTSD are presented in Table 7 for the top and bottom notch ends and represent the displacements perpendicular and parallel to the crack, respectively.

Table 7: Overview of measured CTOD and CTSD together with the FPZ length for top and bottom notch location under pure mode II condition.

Relative notch length a/R [-]	Notch location	Notch inclination angle α [°]	CTOD [μm]	CTSD [μm]	CTSD/CTOD [-]	FPZ length l_{FPZ} [mm]
0.267	Top	27	5.236	16.293	3.11	10.841
0.267	Bottom	27	1.888	6.053	3.21	3.560

The values of CTOD and CTSD as presented in Table 7 are in agreement with the general expectation since the mode II crack sliding component, CTSD has a larger value if compared to the mode I crack opening CTOD component. This validates the observations from in Figure 12 and also provides valuable information about the pure mode II cracking process for concrete. The mode II dominance can be seen in more detail when the ratio of CTSD/CTOD is calculated. Such a ratio shows similar values for both notch ends, which again is in accordance with the observation seen in Figure 12 as the FPZ located at the bottom of the notch did not progress in the same way as the FPZ located at the end of the top notch.

Table 7 presents values of the FPZ length l_{FPZ}, which is the distance from notch tip to the identified location of traction-free crack. Furthermore, if this FPZ size l_{FPZ} is compared with values presented in Table 4, a serious underestimation can be observed. These experimental results again confirm the inapplicability of the fundamental Irwin approach to the estimation of plastic zone r_c for concrete (Eq.3 and Eq. 4), as well as the Hillerborg's analytical formula for the estimations of characteristic length L_{ch} (Eq.5). Similar to this, Bažant's empirical relation of the FPZ size equal to the maximum aggregate size d_{agg} shows closer results if compared to other analytical formulas.

Contrary to this, Irwin's value of the critical distance r_C for plane stress (Eq. 3) predicts the FPZ size to be 3.79 mm, while the measured value for bottom notch is 3.56 mm, which provides the smallest

difference between the experimental and analytical values. This agreement between experimental and analytical prediction is rather unique as previous studies generally show higher values of FPZ lengths [24,70]. The valid reason for this agreement is to be the presence of a coarse aggregate ahead of the crack tip, as well as the aggregate interlock, which can be documented by a higher mode II displacement component CTSD.

This inconsistency in the analytical and empirical formulas, i.e. Eqs. (3)-(5) and d_{max}, for the estimation of the FPZ size, is due to the consideration of only mode I fracture toughness K_{IC} in these analytical formulations. Thus, we do not recommend using these formulas for pure mode II loading conditions.

This is a topic that deserves special attention on its own. Additionally, the analysis of FPZ properties under the pure mode II load conditions is an interesting and open topic, which definitely deserves more attention in future studies.

Conclusions

This experimental study has presented a digital image correlation (DIC) analysis of displacements and strain fields captured on Brazilian disc specimens with central notch (BDCN) made of high-performance concrete (HPC), with a focus placed on the localisation of the traction-free crack and on the identification of the fracture process zone (FPZ) ahead of the crack under a pure mode II (shear) load.

The experimental results showed the development of the FPZ throughout the BDCN test, identified the traction-free crack location, and localised the FPZ extent ahead of the crack tip. The traction-free crack localisation was done by adjustment of the methodology found in literature for mode I cracking. This adjustment was verified by presenting the crack opening displacement obtained from both notch ends. This adjusted methodology for the traction-free crack localisation can be used for other loading conditions.

Since the BDCN specimen has a notch placed in the centre of the disc, two independent FPZs can develop during the fracture test on both notch ends. This requires a separate analysis of each FPZ. When comparing the two FPZs located at both notch ends, a significant difference in their size was observed. This difference is related to crack branching and crack arrest due to the presence of the coarse aggregate ahead of the localised traction-free crack. The crack tip opening (CTOD) and crack tip opening sliding (CTSD) displacements were measured and compared on both notch sides. It was found that the crack tip sliding component CTSD was approximately three times larger than the crack opening CTOD component. This difference in CTOD and CSTD was observed for both notch ends.

Lastly, the measured FPZ length l_{FPZ} was compared with the analytical formulas commonly used in the prediction of its size. These formulas are mostly using the fracture toughness for mode I K_{IC}, which for mode II load provides misleading information. Thus, recently proposed adjustments for mode II cracks using the fracture toughness for mode II K_{IIC} for the prediction of the FPZ size were used. The analytical prediction of the size of the FPZ showed a significant improvement in prediction of the FPZ size when using the mode II fracture toughness K_{IIC} rather than the traditional formulation for mode I cracks. Nevertheless, the mode II fracture failure of concrete is an interesting open topic deserving further investigation.

Acknowledgements

Financial support provided by the Czech Science Foundation under project no. 21-08772S, as well as the Financial support of Programa Operativo FEDER from the Junta de Andalucia (Spain) through grant reference UMA18-FEDERJA-250 is also greatly acknowledged. Industrial support from Bettergy and Dr Nicolas Ordonez is greatly acknowledged, as well as access to different structures and materials in the energy industry. PM also acknowledges financial support of a project: “International mobility of researchers at the Brno University of Technology II” funded by the MŠMT of the Czech Republic with registration no. CZ.02.2.69/0.0/0.0/18_053/0016962.

References

[1] M.F. Kaplan, Crack propagation and the fracture of concrete, in: 11th ed., n.d.: pp. 591–610.

[2] T.L. Anderson, Fracture mechanics: fundamentals and applications, CRC press, 2017.

[3] Y. Jenq, S.P. Shah, Two parameter fracture model for concrete, J Eng Mech. 111 (1985) 1227–1241.

[4] B.L. Karihaloo, P. Nallathambi, Effective crack model for the determination of fracture toughness (KIce) of concrete, Eng Fract Mech. 35 (1990) 637–645. https://doi.org/https://doi.org/10.1016/0013-7944(90)90146-8.

[5] X.U. Shilang, H.W. Reinhardt, Determination of double-K criterion for crack propagation in quasi-brittle fracture, Part II: Analytical evaluating and practical measuring methods for three-point bending notched beams, International Journal of Fracture 1999 98:2. 98 (1999) 151–177. https://doi.org/10.1023/A:1018740728458.

[6] Z.P. Bazant, M.T. Kazemi, Determination of fracture energy, process zone longth and brittleness number from size effect, with application to rock and conerete, International Journal of Fracture 1990 44:2. 44 (1990) 111–131. https://doi.org/10.1007/BF00047063.

[7] X. Hu, K. Duan, X. Hu, K. Duan, Size effect and quasi-brittle fracture: the role of FPZ, International Journal of Fracture 2008 154:1. 154 (2009) 3–14. https://doi.org/10.1007/S10704-008-9290-7.

[8] Z.P. Bažant, Size effect, Int J Solids Struct. 37 (2000) 69–80. https://doi.org/10.1016/S0020-7683(99)00077-3.

[9] Z.P. Bažant, J. Planas, Fracture and Size Effect in Concrete and Other Quasibrittle Materials, Fracture and Size Effect in Concrete and Other Quasibrittle Materials. (2019). https://doi.org/10.1201/9780203756799/FRACTURE-SIZE-EFFECT-CONCRETE-QUASIBRITTLE-MATERIALS-ZDEN.

[10] A. Hillerborg, M. Modéer, P.E. Petersson, Analysis of crack formation and crack growth in concrete by means of fracture mechanics and finite elements, Cem Concr Res. 6 (1976) 773–781. https://doi.org/10.1016/0008-8846(76)90007-7.

[11] Fracture Mechanics of Concrete Structures : Proceedings of the First International Conference on Fracture Mechanics of Concrete Structures (FraMCoS1), held at Beaver Run Resort, Breckenridge, Colorado, USA, 1-5 June 1992., Fracture Mechanics of Concrete Structures. (2003). https://doi.org/10.1201/9781482286847.

[12] B.L. Karihaloo, Fracture Mechanics and Structural Concrete (Concrete Design and Construction Series), Ed. Longman Scientific & Technical. United States. (1995).

[13] K.L. Scrivener, A.K. Crumbie, P. Laugesen, The Interfacial Transition Zone (ITZ) Between Cement Paste and Aggregate in Concrete, Interface Science 2004 12:4. 12 (2004) 411–421. https://doi.org/10.1023/B:INTS.0000042339.92990.4C.

[14] L. Cedolin, S. Dei Poli, I. Iori, Experimental determination of the fracture process zone in concrete, Cem Concr Res. 13 (1983) 557–567. https://doi.org/10.1016/0008-8846(83)90015-7.

[15] L. Cedolin, S.D. Poli, I. Iori, Tensile Behavior of Concrete, J Eng Mech. 113 (1987) 431–449. https://doi.org/10.1061/(ASCE)0733-9399(1987)113:3(431).

[16] S. Muralidhara, B.K.R. Prasad, H. Eskandari, B.L. Karihaloo, Fracture process zone size and true fracture energy of concrete using acoustic emission, Constr Build Mater. 24 (2010) 479–486. https://doi.org/10.1016/j.conbuildmat.2009.10.014.

[17] K. Otsuka, H. Date, Fracture process zone in concrete tension specimen, Eng Fract Mech. 65 (2000) 111–131. https://doi.org/10.1016/S0013-7944(99)00111-3.

[18] I. Kumpova, M. Vopalensky, T. Fila, D. Kytyr, D. Vavrik, M. Pichotka, J. Jakubek, Z. Kersner, J. Klon, S. Seitl, J. Sobek, On-the-Fly Fast X-Ray Tomography Using a CdTe Pixelated Detector - Application in Mechanical Testing, IEEE Trans Nucl Sci. 65 (2018) 2870–2876. https://doi.org/10.1109/TNS.2018.2873830.

[19] I. Kumpova, T. Fila, D. Vavrik, Z. Kersner, X-ray dynamic observation of the evolution of the fracture process zone in a quasi-brittle specimen, Journal of Instrumentation. 10 (2015) C08004. https://doi.org/10.1088/1748-0221/10/08/C08004.

[20] S. Bhowmik, S. Ray, An experimental approach for characterization of fracture process zone in concrete, Eng Fract Mech. 211 (2019) 401–419. https://doi.org/10.1016/J.ENGFRACMECH.2019.02.026.

[21] S. Das, M. Aguayo, G. Sant, B. Mobasher, N. Neithalath, Fracture process zone and tensile behavior of blended binders containing limestone powder, Cem Concr Res. 73 (2015) 51–62. https://doi.org/10.1016/j.cemconres.2015.03.002.

[22] S. Li, X. Fan, X. Chen, S. Liu, Y. Guo, Development of fracture process zone in full-graded dam concrete under three-point bending by DIC and acoustic emission, Eng Fract Mech. 230 (2020) 106972. https://doi.org/10.1016/J.ENGFRACMECH.2020.106972.

[23] X.Z. Hu, F.H. Wittmann, Fracture energy and fracture process zone, Mater Struct. 25 (1992) 319–326. https://doi.org/10.1007/BF02472590.

[24] H. Cifuentes, B.L. Karihaloo, Determination of size-independent specific fracture energy of normal- and high-strength self-compacting concrete from wedge splitting tests, Constr Build Mater. 48 (2013) 548–553. https://doi.org/https://doi.org/10.1016/j.conbuildmat.2013.07.062.

[25] N. Zhang, A. Hedayat, H.G. Bolaños Sosa, J. Tunnah, J.J. González Cárdenas, G.E. Salas Álvarez, Estimation of the mode I fracture toughness and evaluations on the strain behaviors of the compacted mine tailings from full-field displacement fields via digital image correlation, Theoretical and Applied Fracture Mechanics. 114 (2021) 103014. https://doi.org/10.1016/J.TAFMEC.2021.103014.

[26] N. Zhang, A. Hedayat, H.G. Bolaños Sosa, N. Tupa, I. Yanqui Morales, R.S. Canahua Loza, Mechanical and fracture behaviors of compacted gold mine tailings by semi-circular bending tests and digital image correlation, Constr Build Mater. 306 (2021) 124841. https://doi.org/10.1016/J.CONBUILDMAT.2021.124841.

[27] K.N. Rahal, M.P. Collins, Background to the general method of shear design in the 1994 CSA-A23.3 standard, Canadian Journal of Civil Engineering. 26 (1999) 827–839. https://www.proquest.com/scholarly-journals/background-general-method-shear-design-1994-csa/docview/213441503/se-2?accountid=17115.

[28] J. Lee, M. Nishiyama, S. Kono, M. Sakashita, Diagonal Tension Failure of Reinforced and Prestressed Concrete Member, ACI Struct J. 112 (2015) 311–321. https://www.proquest.com/scholarly-journals/diagonal-tension-failure-reinforced-prestressed/docview/1680122564/se-2?accountid=17115.

[29] F. Cavagnis, M. Fernández Ruiz, A. Muttoni, Shear failures in reinforced concrete members without transverse reinforcement: An analysis of the critical shear crack development on the basis of test results, Eng Struct. 103 (2015) 157–173. https://doi.org/10.1016/J.ENGSTRUCT.2015.09.015.

[30] T.N.H. Nguyen, K.H. Tan, T. Kanda, Investigations on web-shear behavior of deep precast, prestressed concrete hollow core slabs, Eng Struct. 183 (2019) 579–593. https://doi.org/10.1016/J.ENGSTRUCT.2018.12.052.

[31] E. Cuenca, P. Serna, Failure modes and shear design of prestressed hollow core slabs made of fiber-reinforced concrete, Compos B Eng. 45 (2013) 952–964. https://doi.org/10.1016/J.COMPOSITESB.2012.06.005.

[32] T. Karmokar, A. Mohyeddin, J. Lee, T. Paraskeva, Concrete cone failure of single cast-in anchors under tensile loading – A literature review, Eng Struct. 243 (2021) 112615. https://doi.org/10.1016/J.ENGSTRUCT.2021.112615.

[33] L.P. Pook, Five decades of crack path research, Eng Fract Mech. 77 (2010) 1619–1630. https://doi.org/10.1016/j.engfracmech.2010.04.010.

[34] L.P. Pook, Crack Paths, WIT Press, 2002. https://books.google.cz/books?id=PuJRAAAAMAAJ.

[35] F. Erdogan, G.C. Sih, On the Crack Extension in Plates Under Plane Loading and Transverse Shear, Journal of Basic Engineering. 85 (1963) 519–525. https://doi.org/10.1115/1.3656897.

[36] G.C. Sih, Strain-energy-density factor applied to mixed mode crack problems, Int J Fract. 10 (1974) 305–321. https://doi.org/10.1007/BF00035493.

[37] The double-edge notched specimen (DENS) applied to study the fracture of concrete under shear loading: experimental approach, (n.d.). https://www.concrete.org/publications/internationalconcreteabstractsportal/m/details/id/51709336 (accessed June 1, 2022).

[38] J.C. Gálvez, M. Elices, G. v. Guinea, J. Planas, Mixed Mode Fracture of Concrete under Proportional and Nonproportional Loading, International Journal of Fracture 1998 94:3. 94 (1998) 267–284. https://doi.org/10.1023/A:1007578814070.

[39] W.W. Ji, P.Z. Pan, Q. Lin, X.T. Feng, M.P. Du, Do disk-type specimens generate a mode II fracture without confinement?, International Journal of Rock Mechanics and Mining Sciences. 87 (2016) 48–54. https://doi.org/10.1016/J.IJRMMS.2016.05.010.

[40] Q. Lin, H. Yuan, L. Biolzi, J.F. Labuz, Opening and mixed mode fracture processes in a quasi-brittle material via digital imaging, Eng Fract Mech. 131 (2014) 176–193. https://doi.org/10.1016/J.ENGFRACMECH.2014.07.028.

[41] F. Ouchterlony, Suggested methods for determining the fracture toughness of rock, in: International Journal of Rock Mechanics and Mining Sciences & Geomechanics Abstracts, 1988: pp. 71–96.

[42] Vic-2D V6 Reference Manual, Correlated Solutions Incorporated (C.S.Inc), (n.d.).

[43] P. Miarka, A.S. Cruces, S. Seitl, L. Malíková, P. Lopez-Crespo, Evaluation of the SIF and T-stress values of the Brazilian disc with a central notch by hybrid method, Int J Fatigue. 135 (2020). https://doi.org/10.1016/j.ijfatigue.2020.105562.

[44] H. Tada, P.C. Paris, G.R. Irwin, A.S. of M. Engineers., A.S.M. International., The stress analysis of cracks handbook, 3rd ed., ASME Press : Professional Engineering Pub. : ASM International, New York, 2000.

[45] S. Seitl, P. Miarka, V. Bílek, The mixed-mode fracture resistance of C 50/60 and its suitability for use in precast elements as determined by the Brazilian disc test and three-point bending specimens, Theoretical and Applied Fracture Mechanics. 97 (2018). https://doi.org/10.1016/j.tafmec.2018.08.003.

[46] T. Tang, S.P. Shah, C. Ouyang, Fracture Mechanics and Size Effect of Concrete in Tension, Journal of Structural Engineering. 118 (1992) 3169–3185. https://doi.org/10.1061/(ASCE)0733-9445(1992)118:11(3169).

[47] T. Tang, Effects of load-distributed width on split tension of unnotched and notched cylindrical specimens, J Test Eval. 22 (1994) 401–409. https://doi.org/10.1520/JTE12656J.

[48] P. Miarka, S. Seitl, V. Bílek, Mixed-mode fracture analysis in high-performance concrete using a Brazilian disc test, Materiali in Tehnologije. 53 (2019). https://doi.org/10.17222/mit.2018.161.

[49] H. Schreier, J.J. Orteu, M.A. Sutton, Image correlation for shape, motion and deformation measurements: Basic concepts, theory and applications, Image Correlation for Shape, Motion and Deformation Measurements: Basic Concepts,Theory and Applications. (2009) 1–321. https://doi.org/10.1007/978-0-387-78747-3.

[50] W.F. Clocksin, J.Q. da Fonseca, P.J. Withers, P.H.S. Torr, Image processing issues in digital strain mapping, in: A.G. Tescher (Ed.), Proceedings of SPIE, Application of Digital Image Processing XXV, 2002: pp. 384–395.

[51] Matlab, version 9.10.0 (R2018a), The MathWorks Inc., 2018.

[52] P. López-Crespo, R.L. Burguete, E.A. Patterson, A. Shterenlikht, P.J. Withers, J.R. Yates, Study of a crack at a fastener hole by digital image correlation, Exp Mech. 49 (2009) 551–559. https://doi.org/10.1007/S11340-008-9161-1/FIGURES/8.

[53] J. Canny, A Computational Approach to Edge Detection, IEEE Trans Pattern Anal Mach Intell. PAMI-8 (1986) 679–698. https://doi.org/10.1109/TPAMI.1986.4767851.

[54] P. Lopez-Crespo, A. Shterenlikht, E.A. Patterson, J.R. Yates, P.J. Withers, The stress intensity of mixed mode cracks determined by digital image correlation:, Journal of Strain Analysis for Engineering Design. 43 (2008) 769–780. https://doi.org/10.1243/03093247JSA419.

[55] P. Lopez-Crespo, A. Shterenlikht, J.R. Yates, E.A. Patterson, P.J. Withers, Some experimental observations on crack closure and crack-tip plasticity, Fatigue Fract Eng Mater Struct. 32 (2009) 418–429. https://doi.org/10.1111/J.1460-2695.2009.01345.X.

[56] M. Zanganeh, P. Lopez-Crespo, Y.H. Tai, J.R. Yates, Locating the Crack Tip Using Displacement Field Data: A Comparative Study, Strain. 49 (2013) 102–115. https://doi.org/10.1111/STR.12017.

[57] L. Chen, G. Zhang, Z. Zou, Y. Guo, X. Zheng, The effect of fracture growth rate on fracture process zone development in quasi-brittle rock, Eng Fract Mech. 258 (2021) 108086. https://doi.org/10.1016/J.ENGFRACMECH.2021.108086.

[58] S. Das, M. Aguayo, V. Dey, R. Kachala, B. Mobasher, G. Sant, N. Neithalath, The fracture response of blended formulations containing limestone powder: Evaluations using two-parameter fracture model and digital image correlation, Cem Concr Compos. 53 (2014) 316–326. https://doi.org/10.1016/J.CEMCONCOMP.2014.07.018.

[59] Z.M. Wu, H. Rong, J.J. Zheng, F. Xu, W. Dong, An experimental investigation on the FPZ properties in concrete using digital image correlation technique, Eng Fract Mech. 78 (2011) 2978–2990. https://doi.org/10.1016/J.ENGFRACMECH.2011.08.016.

[60] G.R. Irwin, Plastic Zone Near a Crack and Fracture Toughness., in: Sagamore Research Conference, 1961: pp. 63–78.

[61] A. Aminzadeh, B. Bahrami, M.R. Ayatollahi, M. Nejati, On the role of fracture process zone size in specifying fracturing mechanism under dominant mode II loading, Theoretical and Applied Fracture Mechanics. 117 (2022) 103150. https://doi.org/10.1016/J.TAFMEC.2021.103150.

[62] Z.P. Bazant, Mechanics of fracture and progressive cracking in concrete structures, Fract Mech of Concr, Struct Appl and Numer Calc. (1985) 1–94. https://doi.org/10.1007/978-94-009-6152-4_1.

[63] K. Otsuka, H. Date, Fracture process zone in concrete tension specimen, Eng Fract Mech. 65 (2000) 111–131. https://doi.org/10.1016/S0013-7944(99)00111-3.

[64] N. Alanazi, L. Susmel, Theory of Critical Distances and static/dynamic fracture behaviour of un-reinforced concrete: length scale parameters vs. material meso-structural features, Eng Fract Mech. 261 (2022) 108220. https://doi.org/10.1016/J.ENGFRACMECH.2021.108220.

[65] Y. Jianhong, F.Q. Wu, J.Z. Sun, Estimation of the tensile elastic modulus using Brazilian disc by applying diametrically opposed concentrated loads, International Journal of Rock Mechanics and Mining Sciences. 46 (2009) 568–576. https://doi.org/10.1016/J.IJRMMS.2008.08.004.

[66] C. Li, VECTOR CTD CRITERION APPLIED TO MIXED MODE FATIGUE CRACK GROWTH, Fatigue Fract Eng Mater Struct. 12 (1989) 59–65. https://doi.org/10.1111/J.1460-2695.1989.TB00508.X.

[67] S. Pommier, P. Lopez-Crespo, P.Y. Decreuse, A multi-scale approach to condense the cyclic elastic-plastic behaviour of the crack tip region into an extended constitutive model, Fatigue Fract Eng Mater Struct. 32 (2009) 899–915. https://doi.org/10.1111/J.1460-2695.2009.01392.X.

[68] J. Tong, R. . Yates, M.W. Brown, A model for sliding mode crack closure part I: Theory for pure mode II loading, Eng Fract Mech. 52 (1995) 599–611. https://doi.org/10.1016/0013-7944(95)00044-V.

[69] J. Tong, J.R. Yates, M.W. Brown, A model for sliding mode crack closure part II: mixed mode I and II loading and application, Eng Fract Mech. 52 (1995) 613–623. https://doi.org/10.1016/0013-7944(95)00045-W.

[70] C. Rosselló, M. Elices, G. v. Guinea, Fracture of model concrete: 2. Fracture energy and characteristic length, Cem Concr Res. 36 (2006) 1345–1353. https://doi.org/10.1016/J.CEMCONRES.2005.04.016.